Automated discrimination of fault scarps along an Arctic mid-ocean ridge using neural networks

Cyril Juliani[1]

Norwegian University of Science and Technology (NTNU), Department of Geoscience and Petroleum, Sem Sælandsvei 1, 7491, Trondheim, Norway

A B S T R A C T

Multibeam bathymetric data, acquired along mid-ocean ridges (MORs), provide critical information for the modeling of seabed terrains and the understanding of related geology. An automated detection of geological features, such as fault structures, helps to elucidate the structural characteristics of MORs and quantify e.g., the magnitude and spatial variability of geological phenomena such as faulting. For this purpose, this research presents a developed cross-sectional methodology where continuous elevation data are (1) collected across a MOR from individual transect lines at various spatial resolutions (50–150 m), and then (2) analyzed with a supervised learning algorithm to discriminate fault structures. An artificial neural network (ANN) is applied for the detection and classification of fault scarps which have either an east or west tilt orientation; the classification uses attributes of elevation data calculated from surface derivation, simulated relief shading and statistical analyses of transects. Results indicate an average detection accuracy of 92%, which is dependent on the data sampling resolution, the terrain complexity and the predictor variables considered. Both the *variance* and *regression slope* variables played a key role in the training phase for identifying and classifying the tectonic features. The cross-sectional learning method presented in this research finally evidences the possibility to achieve an automated quantification system for different landform types and emphasizes the need for complementary classification methods to deepen the interpretation of landform complexities and related geological processes at MORs.

1. Introduction

Fault detection has been treated as a recurrent problem in quantitative geomorphology (e.g., Goff, 1991; Shaw, 1992; Shaw and Lin, 1993; Little and Smith, 1996; Carbotte et al., 2003). Popular techniques used to reveal fault signatures usually consist of segmenting landscapes based on selected ranges of values for given morphometric terrain parameters (e.g., slope, aspect and curvature; Olaya, 2009). At given thresholds, these parameters can filter steep features (Jordan et al., 2005) most often specific to normal slip tectonics responsible for disrupting reliefs at e.g., slow-spreading mid-ocean ridges (MORs) (e.g., Paulatto et al., 2015). At these settings, low spreading rates involve significant tectonic extension and large-throw abyssal hill scarps developing in the flanking tectonic province of the ridge (Whitmarsh and Laughton, 1976; Searle and Laughton, 1977; Macdonald, 1982; Goff, 1991; Shaw and Lin, 1993). These scarps are usually comparable to reliefs produced by vertical fault offsets (e.g., Bates and Jackson, 1987; Escartin et al., 1999) which come with various angles of emergence at

the seafloor (Smith et al., 2008; Lavier et al., 1999), and their characteristic steepness makes them reliable geomorphic indicators of tectonic disruption (Jordan et al., 2005).

A quantitative characterization of these disruptions, with the help of adequate predictor variables, provides early constraints for automated detection. As demonstrated in the literature, fault identification at MORs usually involves thresholding techniques on terrain attributes that are evaluated from large-scale multi-beam bathymetry maps and/or side-scan sonar data (e.g. Searle, 1984; Shaw, 1992; Shaw and Lin, 1993; Carbotte and Macdonald, 1994; Alexander and Macdonald, 1996; Gill, 1998; Scheirer et al., 2000; Carbotte et al., 2003) and, sometimes in conjunction with other imagery data (side-scan backscatter data, videos and photographs), used to map different types of morphologies (e.g., Micallef et al., 2012). While some constrained subsets of slopes (e.g., Shaw and Smith, 1987; Smith and Shaw, 1989) or curvatures (e.g., Shaw, 1992; Shaw and Lin, 1993) as fault indicators, other proposed wavelet-based analyses to infer steep reliefs (Little and Smith, 1996). Because these attempts generally use selective threshold limits
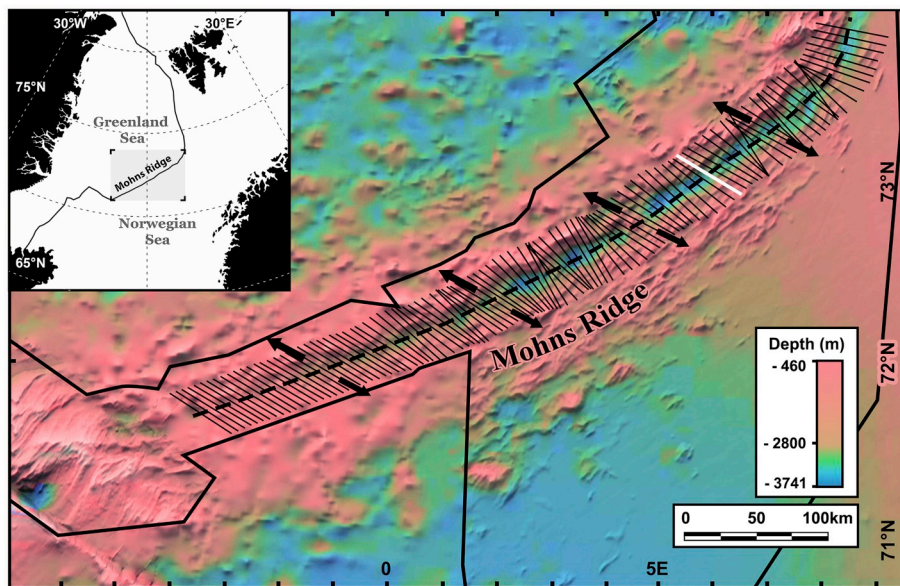

Fig. 1. Location of the study area where multibeam data have been collected (black polygon). The mid-axis of the ridge trend, some examples of transects used as training data and the spreading direction are indicated by a dashed line, straight lines and arrows respectively. The white line corresponds to in-situ investigations (see Fig. 2). Seafloor terrains are analyzed on either side of the ridge axis over 510 km of distance along the ridge. The basemap with shaded relief was taken and modified from GEBCO bathymetry data (http://www.gebco.net/data_and_products/gridded_bathymetry_data/).

to understand the variation of the bathymetry, they identify features in a deterministic way with various degrees of accuracy and recover incomplete geometric information. For example, the upper fault edges of scarp flanges are more likely to be detected, among other steep structures (e.g., volcanic and mass-wasting features), while the downslope reliefs at the scarp end, i.e. where the surface rupture is evidenced by a lineament, usually remain poorly constrained because gravitational collapses move rocks and sediments downslope during faulting (Allerton et al., 1996). These issues are especially pronounced for image processing techniques which rely only on grey-scale images (Jordan et al., 2005), and tend to persist as much of fault extraction is based on relatively low-resolution maps (i.e., from multibeam or side-scan sonar data).

Using elevation data and corresponding derivatives, an experienced geologist can readily recognize the characteristics of disrupted seafloor features being exposed. Visual inspection of fault scarps may be straightforward, even for subtle topographic changes, with the help of e.g., hill-shading techniques (e.g., Horn, 1981; Thelin and Pike, 1991). Unfortunately, most of these scarps have variable exposures which depend essentially on both the geometry of faults and related surface expression. The latter is, however, generally affected by depositional records due to e.g., mass wasting and sedimentation which can lead to subjective assumptions in the traditional hand-picking process of tectonic features. Rather, a more objective approach needs to consider a more profound measure of terrain variability describing the fault exposures. These outcrops have measurable properties (e.g., vertical and horizontal displacements, and dip separation or fault width) which allow to e.g., make statistical analyses of fault populations for estimating regional extensions (tectonic strain) (e.g., Carbotte and Macdonald, 1994; Cowie et al., 1994; Alexander and Macdonald, 1996; Escartin et al., 1999; Parnell-Turner et al., 2016) and, thus, understand the development of MORs.

Machine learning solutions, such as artificial neural networks (ANNs), can solve the general drawbacks generated from the conventional semi-automatic methods cited above. Instead of taking deterministic assumptions, a learning model performs probabilistic evaluations of input data representing the geomorphic surfaces which are generally understood through expert knowledge. In this context, this research proposes (1) to capture relevant (synthetic) data structures, obtained

from surface derivation, relief shading and statistical description of the bathymetry of an ultraslow-spreading MOR, i.e. the Mohns Ridge (71–73°N), and (2) to develop an ANN classifier for learning data patterns related to fault scarps, so that (3) tectonic features can be identified, and subsequently classified given their tilt orientation. Once trained, the classifier discriminates fault scarps, i.e. those facing away from the ridge axis (outward type) and facing toward the ridge axis (inward type); the latter can be affected to some degree by sedimentation and mass wasting events, while the outward type often consists of hummocky-textured lava terrains that formerly erupted at the rift valley floor and were subsequently faulted and rotated outward (Smith et al., 2008). The scarps analyzed in this paper were shown to have relatively unique signatures that distinguish them from plain areas which are generally of sedimentary origin and/or derived from smooth lava flows. To capture and investigate the scarp properties, cross-sectional samplings of elevation data, taken orthogonally to the ridge, are employed. Since the sampling process is made along the entire ridge trend, the synthetic data, representing the structural trends of the Mohns Ridge, are stored into a matrix that will be exploited by the classifier. The relative importance of synthetic data in this matrix will be ranked given their discrimination performance, while potential classification errors, inherent to landform complexities, will be evidenced.

2. Background information

The Mohns Ridge is an ultra-slow spreading MOR that can be described as a deep rifted axial zone with low spreading rates (15–16 mm a^{-1}; Mosar et al., 2002). The ridge trend is orientated approximately N060° (Dauteuil and Brun, 1996) and extends for about 510 km along its axis (Fig. 1). In the axial rift valley, isolated topographic highs, i.e. axial volcanic ridges (AVRs), are separated by deep basins and marked by characteristic morpho-structures (e.g., dome-shaped axial volcanic ridges, grabens, horsts and tilted blocks; Géli et al., 1994; Dauteuil and Brun, 1996), describing the interplay between magmatic supply variations and tectonism. These AVRs often split with large ongoing fault offsets transporting pieces of crust onto the ridge flanks during amagmatic periods when tectonism is the dominant form of spreading (Parson et al., 1993; Searle et al.,

2010). The destruction period of AVRs participates in the development of abyssal hills as crust moves away from the ridge axis through faulting occurring at the median rift valley (e.g., Parson et al., 1993; Macdonald et al., 1996). The rift typically consists of normal faults operating at variable extents (Dauteuil and Brun, 1996; Bruvoll et al., 2009) and triggering mass movements, as shown in the MarMine cruise report describing the western axial valley wall of the Mohns Ridge (Ludvigsen et al., 2016). Sometimes, a large-offset normal fault (detachment fault) accommodates a part of the plate separation along one of the ridge flanks (Escartin et al., 2008; Smith et al., 2008, 2014). This asymmetric configuration is recurrent along the Mohns Ridge since its western ridge flank often presents larger scarp exposures in contrast to the small-offset and sediment-covered faults of the eastern tectonic provinces (Juliani and Ellefmo, 2018).

Bathymetric data of the Mohns Ridge have been collected by the Norwegian Petroleum Directorate in collaboration with the Geological Institute of the Russian Academy of Sciences. Data collection was done in 2000 and 2001 by Fugro-Geoteam using a hull-mounted Simrad EM 120 echo sounder. A multibeam bathymetry map was compiled from it and stored in a regular grid network (square grid) of 50 m cells resolution, using GIS-based software. Because the map resolution is relatively limited, only fault offsets at scales of kilometers and more were evaluated. In addition, as sedimentation, mass movements and volcanism make fault outcrops rather difficult to discriminate, small-scale faults (with offsets < 100 m) were not considered in this study; this reduces the statistical significance of fault trends and related distributions. Besides this, the relief model still provides an exploitable regional morphotectonic view of the study area because this study attempts to solve a large-scale prediction problem.

3. Methodology

3.1. Transect definition

The proposed methodology analyzes geomorphic data through multiple linear profiles (transects) throughout the Mohns Ridge trend (Fig. 1). Transects have the advantage to capture the essential topographic and tectonic information of the contrasting spreading behaviors throughout MORs (e.g., Shaw and Lin, 1993) when drawn parallel to the spreading direction. In this study, however, this direction often deviates locally from the normal of the ridge trend due to some obliquity (i.e. about 30°; Dauteuil and Brun, 1993), and thus, fault exposures do not always face orthogonally to the ridge trend. To handle this problem, the transects are defined at an angle between the normal to the rift trend and the spreading direction (about 110° from North, at least halfway to the Mohns Ridge; Dauteuil and Brun, 1993). This angle was defined after examining manually the approximate centerline of (i) neo-volcanic zones, given the extent of observable volcano-tectonic features such as hummocky ridges and eruptive fissures along the valley floor, the direction of axial high propagation and related small-offset normal faults, and (ii) deep basins between the neo-volcanic zones, given the delineated ridge valley floor, i.e. the deep and spreading terrains limited by major east-west ridge flanks (see Juliani and Ellefmo, 2018 for details). For the latter, the centerline is calculated automatically with the Thiessen Polygon Method (Thiessen, 1911).

The extent of transects does not exceed 25 km on either side of the centerline (~1.6 million year old crust at most); at this distance, faults still present measurable offsets. The distance interval between two transects is 0.3 km, and the vertices, i.e. the sample points where elevation data are collected along each transect, have an interspacing of 100 m. This interspacing tends to simplify the landform and eliminates small-scale features that may interfere with scarps morphologies (e.g.,

minor volcanic constructions, fault blocks and/or wasted materials). In total, 1750 transects cover the 510-km-long ridge trend analyzed, which represents about 874,300 sampled elevation data points.

3.2. Classification procedure

Probabilistic models, such as artificial neural networks (ANNs), can be designed to find and exploit patterns from input data, and make informative decisions correspondingly (see Bishop, 2006 for details). An ANN model assimilates and recognizes characteristics from a training dataset, i.e. a number of representative examples selected for classification, so that when data from new situations (i.e. unknown or unseen data) are processed, an appropriate classification is made depending on how the patterns found match with those learnt from the training set. In this study, the model decides to classify input data that either distinguish fault scarp morphologies or plain areas. The training set consists of exemplar transects for which elevation data were manually classified by interpreting various topographic cross-sections in map-view. Scarps are identified based on representative input variables (13 for this study; see section 3.3.2) which are given a weight value (positive or negative) depending on their relevance for the identification and classification tasks. After being trained, the network analyzes new examples (testing set) to ensure that the trained network does not fit only the training data. The accuracy of feature classification is quantified during training and testing of the network by calculating the estimation errors generated by the model (see section 3.5).

3.3. Variables and feature selection

3.3.1. Subsets of features for training

To avoid biasing the analysis of the classifier toward the selected data, a consistent set of transects were taken at nearly even distance intervals along the ridge axis (i.e. 4 ± 3 km) to ensure that information learned by the network is representative of the broad morpho-structures and not to specific tectonic features of unique landform. Note that scarps at MORs are affected by various types of mass movements (e.g., Allerton et al., 1996; Goff and Tucholke, 1997; Tucholke, 1992; Tucholke et al., 1997; Mitchell et al., 2000; Cannat et al., 2013), which are comparable to rockfalls in onshore environments where fragments of rock break away from cliffs due to weathering, or landslides where rock debris mobilize downhill under the influence of gravity (Korup, 2012). Because no minority class exists in the classification problem of this study, the selection method used to build the training set does not affect the knowledge generalization of classes.

About 9% of the overall dataset (78,687 data points) was used for training and testing, and partitioned into a training set (60%), validation set (20%) and testing set (20%). The validation set identifies the performance of the network after successive repeated process of training and testing to avoid the effect of preferential sampling. Batches of 100 randomly taken transect data were used for each training step; 1 cycle of training is reached after several steps once all the training data have been used by the network. The training experiments were stopped when no further decrease in the prediction error rate improved the learning accuracy (generally occurring over 60 cycles in this study).

3.3.2. Ranking relevant variables

The discrete tendency of elevation data is informative enough to distinguish a specific scarp from its neighboring landform. Description of such tendency is possible after transforming elevation data by e.g., derivation, which allows describing the slope gradient and aspect of landforms, and simulated shading of terrains (Olaya,
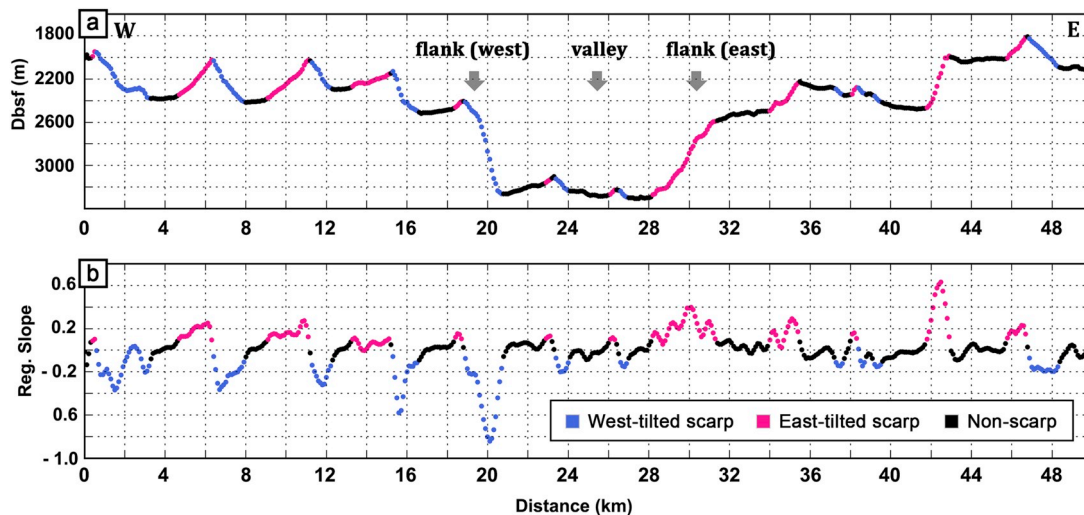
Fig. 2. Example of (a) a transect cross-cutting the spreading ridge between the end of an AVR and a deep basin (white line on Fig. 1); sampled data points have a separation interval of 100 m at distinct depths below sea surface (dbsf) and (b) regression slope calculated from statistical analysis along the transect. The ridge axis is situated at around 25 km of distance from the western transect tip.

2009); the derivation, roughness and shaded relief were calculated in map-view using a GIS software package (see Appendix A). In addition, descriptive statistics of transect vertices (e.g., variance, p-value and regression slope) have been calculated to discretize local landforms by using a fixed-size sliding window. At every point, the window evaluates the statistical significance of a subset of points comprising x_i, the vertex of interest, and the neighboring ones falling into the interval $[x_{i+n}, x_{i-n}]$, with n being the window size. Resulting statistical values, given to each x_i, represent new transformed data. They tend to describe both the vertical extent and the geometry of major tectonic disruptions. For such matter, the choice of a window size is critical because if it is chosen too large (or too small), it can misrepresent the geometry of the landforms. To handle this issue, multiple window sizes have been tested through iterative procedures, and the most satisfactory one for data representation was chosen (i.e. n = 3 in this study) after visual inspection. An example of an evaluated transect is provided in Fig. 2.

The trends of the transformed data can be studied, first to identify scarp and non-scarp morphologies (S_0 and non-S_0 respectively) and then for classifying scarps depending on their tilt orientation, i.e. either westward or eastward (S_1 and S_2 respectively). An overview of useful

predictor variables is presented in Table 1 and their broad correlation is shown graphically through two-dimensional diagrams in Fig. 3. A selective choice on the most relevant variables for the classification task is done in the ANN model during the learning process by weighting (Bishop, 2006). Some variables can have better performance in separating data into distinct categories, i.e. S_1, S_2 and non-S_0 (e.g., the *variance* to identify and the *coefficient of correlation* to classify, as inferred visually on Fig. 3), while others may enhance the data clustering by adding new information once taken with other more "useful" variables (Guyon and Elisseeff, 2003).

3.4. Network setup

Setting up the network required (1) selecting a model architecture, (2) training the network, and (3) evaluating the predictive performance. Prior to being sent as inputs to the network, synthetic data are normalized to make all units roughly comparable to each other. Output variable of the analysis is expressed in ternary format with respect to the presence (S_1 and S_2) or absence of scarps (non-S_0).

Selecting the number of neurons and hidden layers is critical as it affects the quality of predictions (e.g., Shibata and Ikeda, 2009;

Table 1

Synthetic variables generated from terrain attributes and statistical measures of elevation data.

Variable	Description	Task
Roughness[a]	Ratio between a surface area (landform) sampled locally and the planar area of that surface.	Identify
Slope gradient[a]	Squared maximum rate of change in depth values.	Identify
Variance[b]	Measures how far data set is spread out or how much the values vary from one another (variability of the observations).	Identify
p-value[b]	Two-sided p-value for a hypothesis test whose null hypothesis is that the slope is zero.	Identify
Standard Error[b]	Measure of the accuracy of prediction, i.e. the average distance that the observed values deviate from the true mean (variability of the estimator).	Identify
Aspect[a]	Downslope direction of the maximum rate of change (measured clockwise from North).	Classify
Coefficient of correlation[b]	Amount of variability relative to the mean.	Classify
Regression slope[b]	Slope of the regression line of the standardized data points.	Classify
Intercept[b]	Regression slope intercept.	Classify
Hillshade (N315°)[a]	Shaded relief from a surface raster by considering the illumination source angle (from North) and shadows[c].	Classify
Hillshade (N135°)[a]		
Hillshade (N225°)[a]		
Hillshade (N045°)[a]		

[a] Calculated in map-view using a GIS-based software.

[b] Calculated from linear regressions on data in discrete sliding windows across transects.
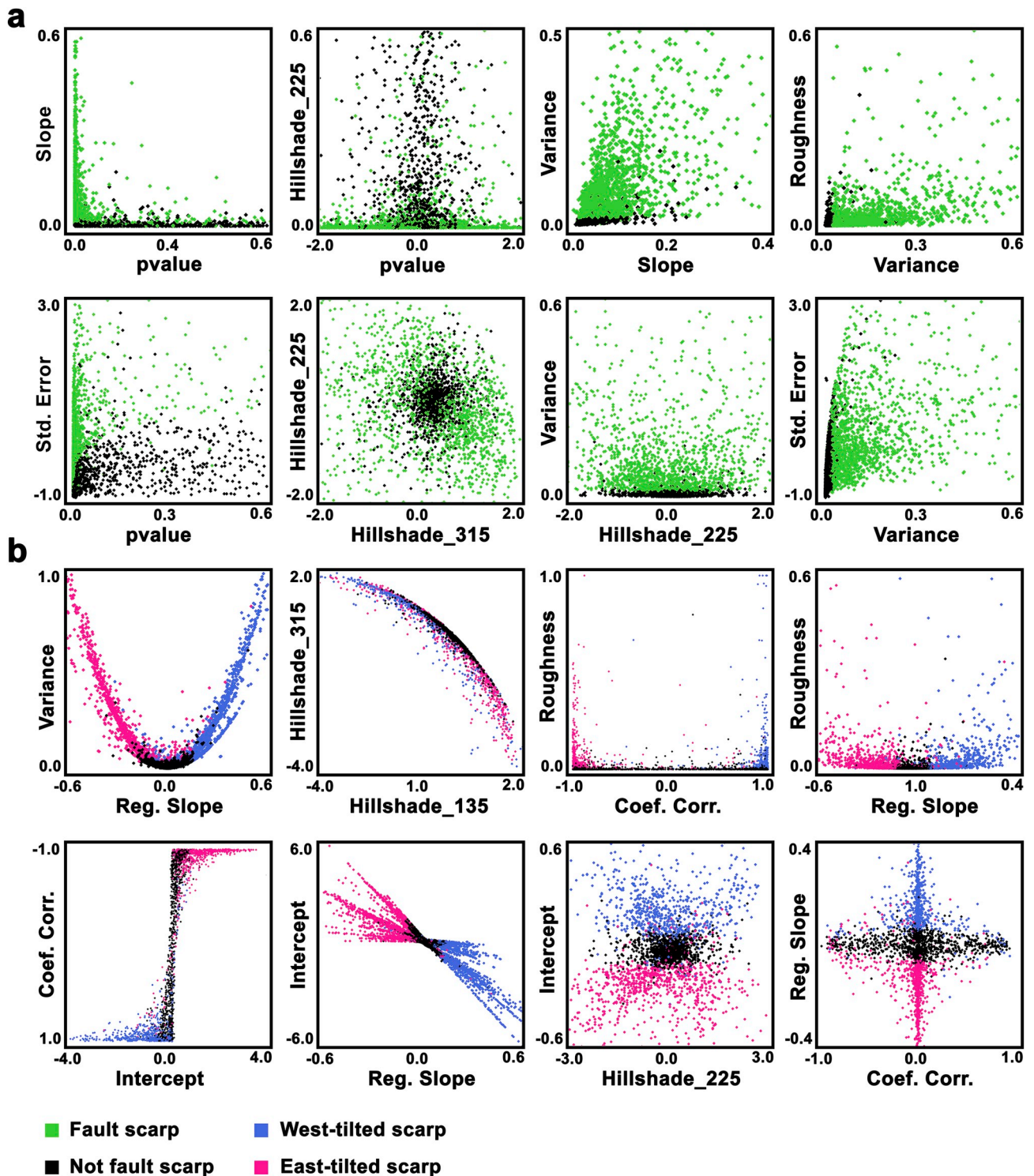
[c] The lighting is at an elevation angle of 45°.

Fig. 3. Examples of scatter plots indicating the relevance of variables for (a) identification and (b) classification tasks.

Karsoliya, 2012). Because this study solves a multi-class classification problem (i.e., 3 possible outputs) and, considering the high dimensionality of the dataset being used (13 variables), both the predictive accuracy and cost function error of the network were estimated iteratively using various numbers of hidden layers (up to 3) and neurons. To decide on the number of hidden layers and neurons, a cross-validation method was applied (Moody, 1994) where networks of different size are trained and evaluated iteratively using a dataset divided in two parts, namely the training set and the validation set. The rule of thumb method was used (Boger and Guterman, 1997; Berry and Linoff, 1997) to choose the number of hidden neurons estimated being in the range between the size of the input layer and the size of the output layer. The number of hidden layers and neurons was finally decided given the estimated model errors obtained from the iteration process.

The training was done using the back-propagation method for

optimization task, with a learning rate of 0.3. The learning rate controls how much we are adjusting the weights of our network in order to minimize the network's loss function (Bishop, 2006). Its value was decided based on the minimum estimation error calculated after successive training tests. The logistic function rectifier linear unit (ReLU) (Nair and Hinton, 2010) was taken as an activation function to increase the non-linear properties of the network. For the classification task, the softmax activation function was used (Bridle, 1990) to assign probabilities to each class of the output and, then, the algorithm was optimized by minimizing the cross-entropy loss (Rubinstein, 1999, 2001). The training procedure has been repeated multiple times to capture the highest average accuracy over a subset of samples taken randomly in the main dataset. For this purpose, a number of transects was selected, then their characteristic data were shuffled and partitioned among the training and validation sets. To avoid overfitting, a regularization term was applied to penalize the large weights (i.e., using the L2-norm solution; Chen and Haykin, 2002) in the neural network. An independent evaluation of the performance was done by presenting the testing data to the network to compute an average accuracy. The entire dataset was finally presented to the trained network to predict fault scarps (S_1 and S_2) separated from the plain terrain (non-S_0). The predicted seafloor structures were finally inspected visually on the bathymetry.

3.5. Metrics and parameters

Evaluating the classification performances requires informative measures such as accuracy, but also specificity and recall. These metrics are commonly used to test capabilities of classification algorithms to detect true and false positives (e.g., the proportion of true and false scarps S_0 recognized respectively) and negatives (e.g., the proportion of true and false non-S_0 terrains recognized respectively) (Sokolova and Lapalme, 2009). The accuracy measures the number of correct predictions, i.e. the total proportion of true positives and true negatives, from all predictions made. Alone, this measure is not enough to make clear judgment on how well the classifier performs as, if the negatives largely overcome the positives in a dataset, a classifier that underestimates the dataset may effectively predict the negatives but not the positives. This tends to increase the overall accuracy of the predictions without yielding the relevant information sought. For this reason, the recall and specificity are also calculated. While the former measures how good the classifier is at detecting the positives, i.e. the occurrences of scarps S_1 and S_2 in this study, the latter measures the proportion of negatives correctly identified by the classifier, i.e. the non-scarp landform S_0. These evaluation metrics are applied during the training and testing phases. They are expressed as follows (Sokolova and Lapalme, 2009):

$$Accuracy = \frac{TN + TP}{TP + FN + TN + FP}$$

$$Recall = \frac{TP}{TP + FN}$$

$$Specificity = \frac{TN}{TN + FP}$$

Table 2
Metrics for identification task of classifier during the training and testing phases at different vertex intervals of individual transects.

Metrics	Training			Testing		
	100 m	50 m	150 m	100 m	50 m	150 m
Accuracy (%)	92.02	85.94	85.41	93.39	87.30	85.69
Specificity (%)	96.87	93.63	82.41	96.82	93.30	80.68
Recall (%)	89.92	83.15	93.77	91.67	84.86	95.00

with TN, TP, FN, FP as true negatives, true positives, false negatives and false positives respectively

4. Results and discussion

4.1. Training and testing

The simplest form of network that generated the smallest generalization error (i.e., 0.217) through the cross-validation method was one hidden layer with 8 neurons. Adding more layers made negligible difference to the prediction accuracy. The average accuracies for the training and testing were 92% and 93% respectively; the former was achieved after 60 cycles of training and did not improve over further training cycles.

Different network adjustments have been tested to obtain a framework that captures the scarps with the highest accuracy. Because the classifier tends to discriminate landforms for fixed vertex sets, transects with increased and decreased vertex intervals (i.e., 150 and 50 m, instead of the 100 m originally applied; see section 3.1) were also analyzed by the trained network to check how spatial resolution affects the resulting classification. Results can be found in Table 2 for the three types of metrics. A clear decline in the average accuracy happens when the distance between vertices differs by ± 50 m (85–93%). Furthermore, recall and specificity have slightly distinct behaviors. While the classifier effectively identifies negative classes up to 100 m interval (> 93%), it declines for a higher vertex interval (< 85%) such that a negative correlation exists between the degree of landform complexity and the non-scarp features (false positives) detected. Recall, on the other hand, presents a different pattern: the determination of relevant information (false negative) increases while morphological details decrease (83–95% for 50- to 150-m interval respectively). This balance between the level of detail and conciseness of scarp identification suggests that the depiction of terrain variation not only depends on terrain attributes but also on spatial resolution. This dependence is corroborated by the contrasting performance shown between specificity and recall at 50-m and 150-m intervals (Table 2).

The learning gap (8%) can be seen as the changing landforms remaining to be learnt, or as the missing information that may improve the predictions. A major issue is the considerable structural control on debris generation in the study area that locally complicates the topography, and thus, induces incomplete identifications of fault scarp morphologies (Fig. 4b). The recall and specificity, calculated for different vertex intervals (Table 2), illustrate this complexity in the topography: too detailed (50-m distance), the model tends to underestimate the observations, i.e. with higher specificity and lower recall, while simpler landform makes the classifier overestimate its analysis, i.e. with higher recall and lower specificity, because larger vertex distances (> 100 m) effectively reduce the influence of spatial heterogeneity present in the landform. The 100-m vertex interval has the advantage to reduce the processing time needed for data integration and classification. To avoid any overestimation, however, a topographic smoothing with appropriate filters may also be suggested prior to extracting the datasets, at the expense of losing the details of scarp ends, because a smoothing would attenuate the fine variations of the elevation data.

4.2. Classification and limitations

Fig. 4 shows heatmap visualizations of the target scarps generated from the neural network model, and classified escarpments are shown in Fig. 5. Even though the overall scarps are correctly identified, the performance of the identifier differs depending on the vertex interval chosen. The identification accuracy declines toward 50% or below with low terrain detailing (150 m) (Fig. 4d) while
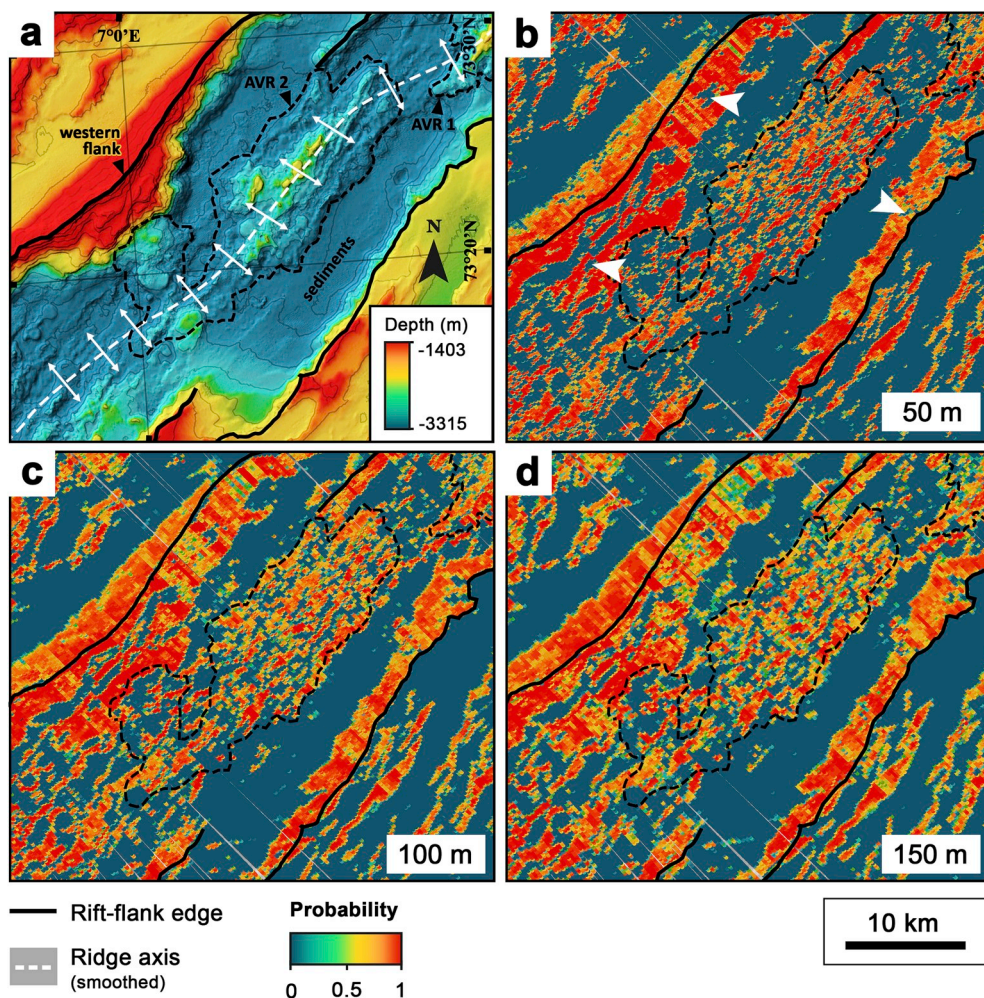
Fig. 4. Visual comparison of discriminated scarps from (a) a section of the bathymetry located in the northern region of the Mohns Ridge. Probabilities of identified scarps are shown for (b) 50-m, (c) 100-m, and (d) 150-m spatial resolutions, and corresponding classification is presented on Fig. 5. The white arrows indicate the transect direction in (a) and examples of unidentified fault exposures in (b) where local structuration is more complex. The ridge axis was taken on the basis of the bathymetric data, given the approximate centerline of the AVR and/or the centerline of the ridge valley delimited by the western and eastern major fault edges (see section 3.1 for details). Interval of the depth contours is 150 m. AVR: axial volcanic ridge.

higher resolution (50 m) provides better discriminations (> 90%; Fig. 4b). For the latter, scarps are more precisely distinguished, but such distinction sometimes makes a partial identification of the scarp-related reliefs (see Fig. 4b), notably usually those modified by mass wasting events (e.g., Tucholke, 1992; Tucholke et al., 1997) or hidden by long-term pelagic sedimentation and talus accumulation (e.g., Searle et al., 1998). These terrains are not markedly discriminated from the descriptive statistics and derivatives of the elevation data as the landform tends to flatten. The use of higher vertex intervals, however, reduces these irregularities because as sampled data points are more distanced, their statistical description tends to disregard smaller landform details. While this may contribute to detect the wasted materials of scarps, it may also include

some false positives, notably volcanic structures, which are generally more preponderant in the ridge valley and can be treated falsely as tectonic offsets. For these reasons, post-processing corrections are necessary to reduce general errors related to landform variabilities. For example, identified fault scarp extents can be individually analyzed in terms of geometry (e.g., length, heave, vertical throw and tilt angle) and compared with a neighboring scarp population (from neighboring transects) or with statistical measures of the overall detected scarps, so that uncommon fault offsets in a given region may be considered for removal.

In addition, tectonic features such as well-rotated large-offset detachment faults generally develop curved oceanic core complexes (OCCs) with low-angle fault offsets (Smith et al., 2008). These are
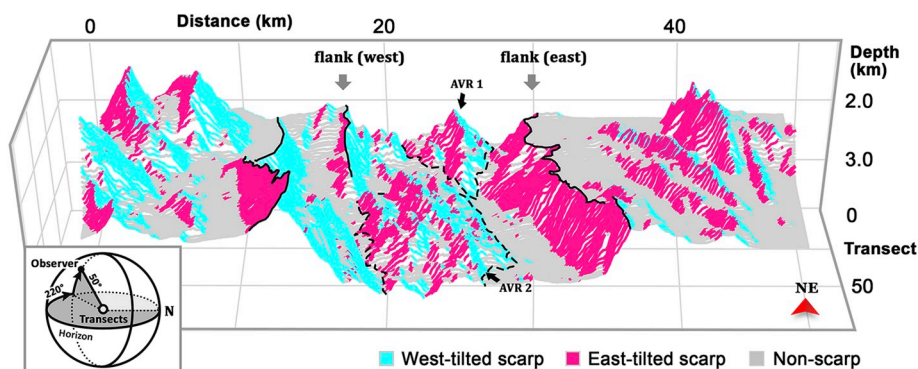

Fig. 5. Examples of 100 transects with classified scarps shown in a 3-dimensional view. Observation is made at an elevation of 50° from the horizontal plan and toward the north-east (NE) at an azimuth of 220° from North. The ridge axis is at around 25 km of distance from the westernmost border of the topography. The ridge valley is delimited by its two high-relief flanks (west and east) and consists of two axial volcanic ridges (AVRs).
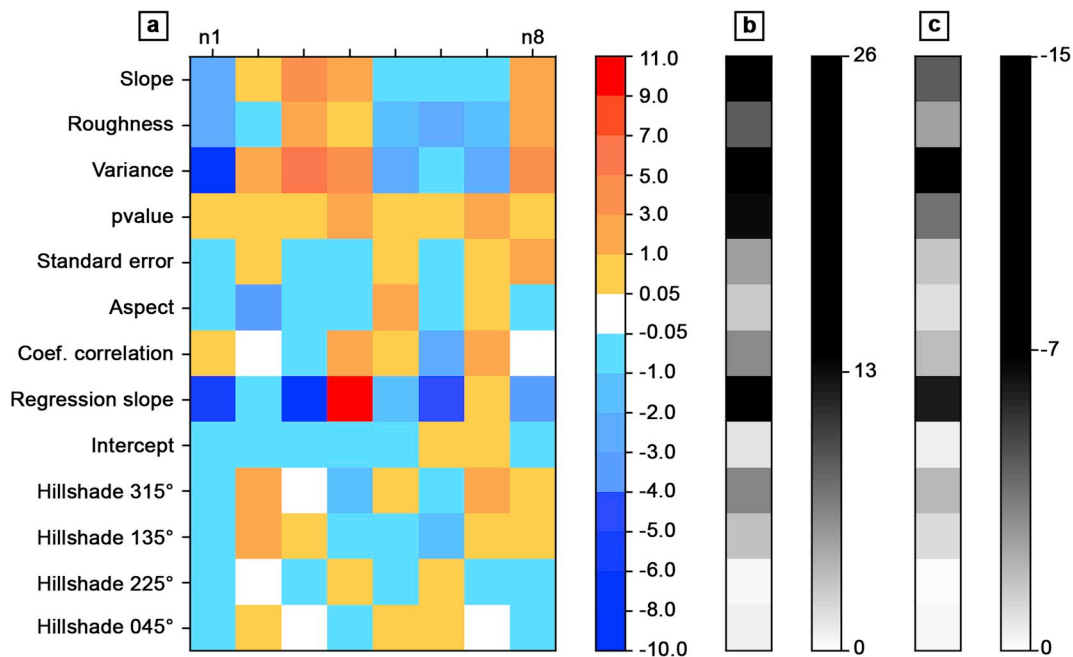
Fig. 6. Weight matrix of the input layer (a) with rows and columns representing source of inputs and destination neurons respectively. The sum of positive (b) and negative weights (c) yield the heterogeneous connection weight distribution in the overall matrix; they respectively correspond to excitatory and inhibitory connectivities.

not completely depicted along the Mohns Ridge by the cross-sectional learning method presented in this study as this method relates mostly on outcrops displaying more or less straight (non-curved) escarpments. Therefore, new informative data, possibly with other sampling-based classifiers, should be considered to recognize these exposed detachment faults.

4.3. Relevance of variables

To determine the relevance of the variables, one can investigate how the trained network attributes weight to each of the destination neurons (Fig. 6). The connection weight matrix of the input layer shows more emphasis on the *variance* and the *regression slope* variables through very distinct maxima (−10 to 11; Fig. 6a) and summed positive and negative weights (above 10 and below −10 respectively; Fig. 6b and c) among the destination neurons. These two variables thus seem to capture the overall relevant information for scarp identification and classification. On the other hand, the *slope* and the *pvalue*, and to some extent the *coefficient of correlation* and the *roughness*, complement this tendency with positive and negative connection weights of a distinct order of magnitude (up to 5 and down to −4 respectively) (Fig. 6a). Among these variables, one observable aspect of the distributed synaptic weights is the complementarity between the *slope*, the *roughness* and the *variance* (Fig. 6a) through which a positive correlation may be implied. Although these correlated variables can be identified as redundant information for the learning process, the classifier here selectively eliminates or emphasises some of the given inputs by weighting. Other elements, with less influence on the output neurons (e.g., the *standard error*, the *intercept* and the *shaded relief* data), have a tendency to be linked with minor weight variations which assume that they have complementary roles rather than being determinant in the predictions. The above-mentioned variables have thus a tendency to be linked with excitatory or inhibitory connections in the trained network which suggests connection neurons of distinct functions reserved for either identification and/or classification tasks.

5. Conclusion

A cross-sectional methodology, combined with a supervised learning algorithm, was applied to discriminate fault segments along a MOR, at different resolutions (50, 100 and 150 m). Results showed that classification errors relate mainly to both (1) the morphological complexity of bathymetric data due notably to mass movements and/or fault geometries, and (2) the choice of sampling scale which depends on both the resolution of survey data and the size of the features sought. Characteristic variables, such as the *variance* and the *regression slope*, made the classification process readily accurate (92%) with the help of complementary data described by e.g., the *slope*, the *coefficient of correlation*, the *pvalue* and the *roughness*.

The cross-sectional method used in this research allows flexible manipulation of bathymetric data. These data could be processed to (1) quantify seafloor structures, such as fault scarp components (e.g., the width, heave and vertical throw, and the dipping angle) from which the regional extension (tectonic strain) can be deduced, and (2) understand the importance of these structures for seafloor spreading throughout a MOR. The detection of other types of geological features (e.g., volcanic structures and fault-related mass-wasting deposits) with detection algorithms complementing the method presented in this study, may also help refining our understanding of spreading processes at MORs.

Acknowledgements
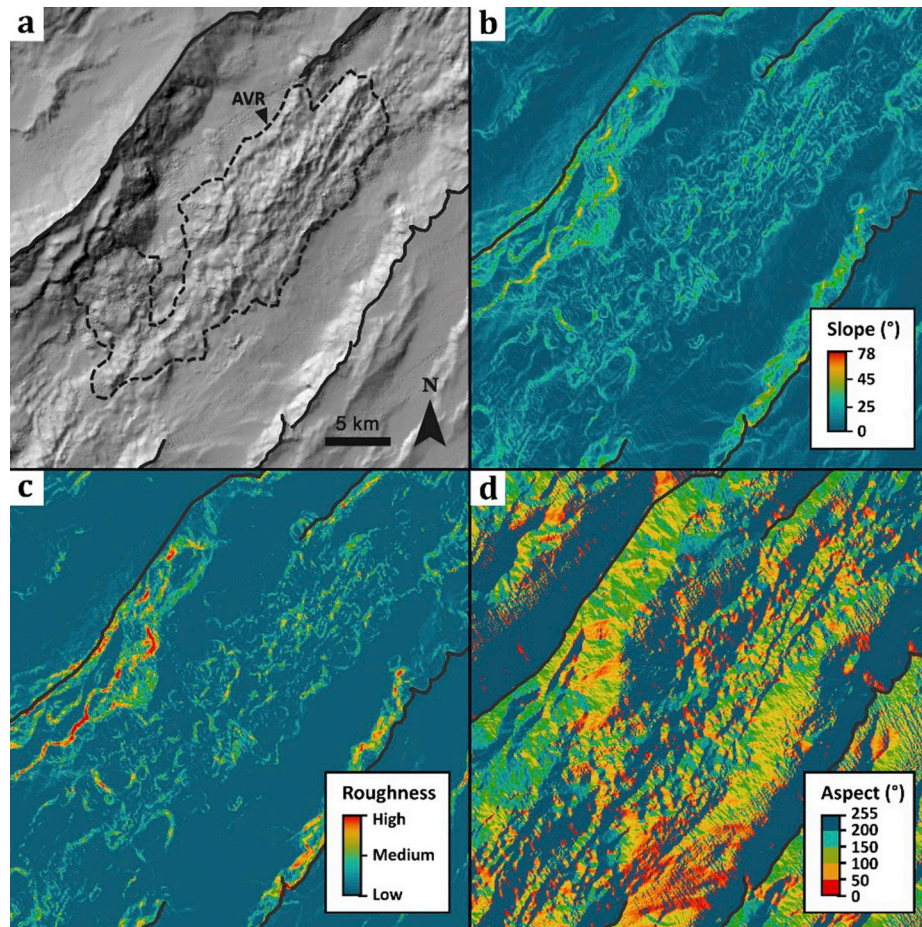
Appendix A. Terrain analysis

Fig. A1. Examples of (a) grey-scale shading of terrain with a lighting azimuth of 315° and an altitude of 45°, (b) slope gradient, (c) roughness and (d) aspect calculated for a segment of the northern region of the Mohns Ridge (characterized in Fig.4). Dark lines indicate the major fault edges at the ridge valley flanks.

Appendix B. Supplementary data

Supplementary data to this article can be found online at https://doi.org/10.1016/j.cageo.2018.12.010.

References

Alexander, R.T., Macdonald, K.C., 1996. Sea beam, sea MARC II and ALVIN-based: studies of faulting on the east Pacific Rise 9°20'N-9°50'N. Mar. Geophys. Res. 18, 557–587.

Allerton, S., Searle, R.C., Murton, B.J., 1996. Bathymetric segmentation and faulting on the mid-Atlantic ridge, 24°00'N to 24°40'N. Geol. Soc. Lond. Spec. Publ. 118 (1), 49–60.

Bates, R.L., Jackson, J.A., 1987. Glossary of Geology, third ed. American Geological Institute, Alexandria, Virginia, pp. 788.

Berry, M.J.A., Linoff, G., 1997. Data Mining Techniques for Marketing, Sales, and Customer Relationship Management. Wiley, pp. 888.

Bishop, C.M., 2006. Pattern Recognition and Machine Learning. Springer, pp. 758.

Boger, Z., Guterman, H., 1997. Knowledge extraction from artificial neural network models. In: IEEE Systems, Man, and Cybernetics Conference, Orlando, FL, . https://doi.org/10.1109/ICSMC.1997.633051.

Bridle, J.S., 1990. Training stochastic model recognition algorithms as networks can lead to maximum mutual information estimation of parameters. In: In: Touretzky, D. (Ed.), Advances in Neural Information Processing Systems, vol. 2. pp. 211–217.

Bruvoll, V., Breivik, A.J., Mjelde, R., Pedersen, R.B., 2009. Burial of the Mohn-Knipovich seafloor spreading ridge by the bear island fan: time constraints on tectonic evolution from seismic stratigraphy: tectonic of the Mohn/Knipovich bend. Tectonics 28, TC4001.

Cannat, M., Mangeney, A., Ondréas, H., Fouquet, Y., Normand, A., 2013. High-resolution bathymetry reveals contrasting landslide activity shaping the walls of the Mid-Atlantic Ridge axial valley. Geochem. Geophys. Geosyst. 14 (4), 996–1011.

Carbotte, S.M., Macdonald, K.C., 1994. Comparison of seafloor tectonic fabric at intermediate, fast and superfast spreading ridges: influence of spreading rate, plate motions, and ridge segmentation on fault patterns. J. Geophys. Res. 99, 13609–13632.

Carbotte, S.M., Ryan, W.B.F., Jin, W., Cormier, M., Bergamis, E., Sinton, J., White, S., 2003. Magmatic subsidence of the East Pacific Rise (EPR) at 18°14'S revealed through fault restoration of ridge crest bathymetry. Geochem. Geophys. Geosyst. 4.

Chen, Z., Haykin, S., 2002. On different facets of regularization theory. Neural Comput. 14, 2791–2846. https://doi.org/10.1162/089976602760805296.

Cowie, P.A., Malinverno, A., Ryan, W.B.E., Edwards, M.H., 1994. Quantitative fault studies on the east Pacific Rise: a comparison of sonar imaging techniques. J. Geophys. Res. 99, 15205–15218.

Dauteuil, O., Brun, J.P., 1996. Deformation partitioning in a slow spreading ridge undergoing oblique extension: Mohns Ridge, Norwegian Sea. Tectonics 15, 870–884.

Dauteuil, O., Brun, J.-P., 1993. Oblique rifting in a slow-spreading ridge. Nature 361, 145–148.

Escartin, J., Cowie, P.A., Searle, R.C., Allerton, S., Mitchell, N.C., MacLeod, C.J., Slootweg, A.P., 1999. Quantifying tectonic strain and magmatic accretion at a slow-spreading ridge segment, Mid-Atlantic Ridge, 29°N. J. Geophys. Res. 104, 10421–10437.

Escartin, J., Smith, D.K., Cann, J., Schouten, H., Langmuir, C.H., Escrig, S., 2008. Central role of detachment faults in accretion of slow-spreading oceanic lithosphere. Nature 455, 790–795.

Géli, L., Renard, V., Rommevaux, C., 1994. Ocean crust formation processes at very slow spreading centers: a model for the Mohns Ridge, near 72°N, based on magnetic, gravity, and seismic data. J. Geophys. Res. 99, 2995–3013.

Gill, J.F., 1998. An Automated Survey of Faulting at the Reykjanes Ridge Using Digital Image Processing Techniques on Gridded Bathymetry Data. MSc thesis. University of Durham.

Goff, J.A., 1991. A global and regional analysis of near-ridge abyssal hill morphology. J.

Geophys. Res. 96, 21713–21737.

Goff, J.A., Tucholke, B.E., 1997. Multiscale spectral analysis of bathymetry on the flank of the Mid-Atlantic Ridge: modification of the seafloor by mass wasting and sedimentation. J. Geophys. Res. 102, 15,447–15,462.

Guyon, I., Elisseeff, A., 2003. An introduction to variable and feature selection. J. Mach. Learn. Res. 3, 1157–1182.

Horn, B.K.P., 1981. Hill shading and the reflectance map. Proc. IEEE 69 (1), 14–47.

Jordan, G., Meijninger, B.M.L., Van Hinsberg, D.J.J., Meulenkamp, J.E., Van Dijk, P.M., 2005. Extraction of morphotectonic features from DEMs: development and applications for study areas in Hungary and NW Greece. Int. J. Appl. Earth Obs. Geoinf. 7, 163–182.

Juliani, C., Ellefmo, S.L., 2018. Probabilistic estimates of permissive areas for undiscovered seafloor massive sulfide deposits on an Arctic Mid-Ocean Ridge. Ore Geol. Rev. 95, 917–930.

Karsoliya, S., 2012. Approximating number of hidden layer neurons in multiple hidden layer BPNN architecture. Int. J. Eng. Trends Technol. 3, 714–717.

Korup, O., 2012. Landslides in the earth system. In: Clague, J.J., Stead, D. (Eds.), Landslides: Types, Mechanism and Modeling. Cambridge University Press, pp. 345–358.

Lavier, L.L., Buck, W.R., Poliakov, A.N.B., 1999. Self-consistent rolling-hinge model for the evolution of large-offset low-angle normal faults. Geology 27, 1127–1130.

Little, S.A., Smith, D.K., 1996. Fault scarp identification in side-scan sonar and bathymetry images from the Mid-Atlantic Ridge using wavelet-based digital filters. Mar. Geophys. Res. 18, 741–755.

Ludvigsen, M., Aasly, K., Ellefmo, S.L., Hilário, A., Ramirez-Llodra, E., Søreide, F.X., Falcon-Suarez, I., Juliani, C.J., Kieswetter, A., Lim, A., Christian, M., Nornes, S.M., Reimers, H., Paulsen, E., Sture, Ø., 2016. MarMine Cruise Report: Arctic Mid-ocean Ridge 15.08.2016 - 05.09.2016. . https://brage.bibsys.no/xmlui/handle/11250/2427715.

Macdonald, K.C., Fox, P.J., Alexander, R.T., Pockalny, R., Gente, P., 1996. Volcanic growth faults and the origin of Pacific abyssal hills. Nature 380, 125–129.

Macdonald, K.C., 1982. Mid-ocean ridges: fine scale tectonic, volcanic and hydrothermal processes within the plate boundary zone. Annu. Rev. Earth Planet Sci. 10, 155–190.

Micallef, A., Le Bas, T.P., Huvenne, V.A.I., Blondel, P., Hühnerbach, V., Deidun, A., 2012. A multi-method approach for benthic habitat mapping of shallow coastal areas with high-resolution multibeam data. Cont. Shelf Res. 39–40, 14–26.

Mitchell, N.C., Tivey, M.A., Gente, P., 2000. Seafloor slopes at mid-ocean ridges from submersible observations and implications for interpreting geology from seafloor topography. Earth Planet. Sci. Lett. 183, 543–555.

Moody, J., 1994. Prediction risk and architecture selection for neural net-works, in statistics to neural networks: theory and pattern recognition applications. In: Cherkassky, V., Friedman, J.H., Wechsler, H. (Eds.), Statistics to Neural Networks: Theory and Pattern Recognition Applications. Springer-Verlag, New York, pp. 147–165 NATO ASI Series F Eds., 136.

Mosar, J., Lewis, G., Torsvik, T.H., 2002. North Atlantic sea-floor spreading rates: implications for the Tertiary development of inversion structures of the Norwegian–Greenland Sea. J. Geophys. Soc. Lond. 159, 503–515.

Nair, V., Hinton, G.E., 2010. Rectified linear units improve restricted Boltzmann machines. In: Proceedings of the 27th International Conference on Machine Learning, pp. 807–814.

Olaya, V., 2009. Chapter 6: basic land-surface parameters. Dev. Soil Sci. 33, 141–169.

Parnell-Turner, R., Schouten, H., Smith, D.K., 2016. Tectonic structure of the mid-Atlantic ridge near 16°30′N. Geochem. Geophy. Geosyst. 17, 3993–4010.

Paulatto, M., Canales, J.P., Dunn, R.A., Sohn, R.A., 2015. Heterogeneous and asymmetric crustal accretion: new constraints from multibeam bathymetry and potential field data from the Rainbow area of the Mid-Atlantic Ridge (36°15′N). Geochem. Geophys.

Geosyst. 16. https://doi.org/10.1002/2015GC005743.

Parson, L.M., Murton, B.J., Searle, R.C., Walker, C., 1993. En-échelon axial volcanic ridges at the Reykjanes Ridge: a life cycle of volcanism and tectonics. Earth Planet. Sci. Lett. 117, 73–87.

Rubinstein, R.Y., 1999. The cross-entropy method for combinatorial and continuous optimization. Methodol. Comput. Appl. Probab. 1, 127–190.

Rubinstein, R.Y., 2001. Combinatorial optimization, cross-entropy, ants and rare events. In: Uryasev, S., Pardalos, P.M. (Eds.), Stochastic Optimization: Algorithms and Applications, pp. 304–358.

Scheirer, D.S., Fornari, D.J., Humphris, S.E., Lerner, S., 2000. High-resolution seafloor mapping using the DSL-120 sonar system: quantitative assessment of sidescan and phase-bathymetry data from the Lucky Strike segment of the Mid-Atlantic Ridge. Mar. Geophys. Res. 21, 121–142.

Searle, R.C., Murton, B.J., Achenbach, K., LeBas, T., Tivey, M., Yeo, I., Cormier, M.H., Carlut, J., Ferreira, P., Mallows, C., Morris, K., Schroth, N., vam Calsteren, P., Waters, C., 2010. Structure and development of an axial volcanic ridge: mid-Atlantic Ridge, 45°N. Earth Planet. Sci. Lett. 2999, 228–241.

Searle, R.C., Cowie, P.A., Mitchell, N.C., Allerton, S., MacLeod, C.J., Escartin, J., Russell, S.M., Slootweg, P.A., Tanaka, T., 1998. Fault structure and detailed evolution of a slow spreading ridge segment: the Mid-Atlantic Ridge at 29°N. Earth Planet. Sci. Lett. 154, 167–183.

Searle, R., 1984. GLORIA survey of the east Pacific Rise near 3.5°S: tectonic and volcanic characteristics of a fast spreading mid-ocean ridge. Tectonophysics 101, 319–344.

Searle, R.C., Laughton, A.S., 1977. Sonar studies of the mid- Atlantic ridge and Kurchatov fracture zone. J. Geophys. Res. 82, 5313–5328.

Shaw, P.R., Lin, J., 1993. Causes and consequences of variations in faulting style at the Mid-Atlantic Ridge. J. Geophys. Res. 98 (B12), 21839–21851.

Shaw, P.R., 1992. Ridge segmentation, faulting and crustal thickness in the Atlantic ocean. Nature 358, 490–493.

Shaw, P.R., Smith, D.K., 1987. Statistical methods for describing seafloor topography. Geophys. Res. Lett. 14, 1061–1064.

Shibata, K., Ikeda, Y., 2009. Effect of number of hidden neurons on learning in large-scale layered neural networks. In: Proceedings of the ICROS-SICE International Joint Conference 2009 (ICCAS-SICE '09), pp. 5008–5013.

Smith, D.K., Shaw, P.R., 1989. Using topographic slope distribution to infer seafloor patterns. IEEE J. Ocean. Eng. 14, 338–347.

Smith, D.K., Escartín, J., Schouten, H., Cann, J.R., 2008. Fault rotation and core complex formation: significant processes in seafloor formation at slow-spreading mid-ocean ridges (Mid-Atlantic Ridge, 13–25°N). Geochem. Geophys. Geosyst. 9, Q03003.

Smith, D.K., Schouten, H., Dick, H.J.B., Cann, J.R., Salters, V., Marschalll, H.R., Ji, F., Yoerger, D., Sanfilippo, A., Parnell-Turner, R., Palmiotto, C., Zheleznov, A., Bai, H., Junkin, W., Urann, B., Dick, S., Sulanowska, M., Lemmond, P., Curry, S., 2014. Development and evolution of detachment faulting along 50 km of the Mid-Atlantic Ridge near 16.5°N. Geochem. Geophys. Geosyst. 15, 4692–4711.

Sokolova, M., Lapalme, G., 2009. A systematic analysis of performance measures for classification tasks. Inf. Process. Manag. 45, 427–437.

Thelin, P., Pike, R., 1991. Landforms of the conterminous United States - a digital shaded-relief portrayal. Technical Report I-2206. U.S. Geological Survey Miscellaneous Investigations Series Map (map and accompanying text), pp. 16.

Thiessen, A.H., 1911. Precipitation for large areas. Mon. Weather Rev. 39, 1082–1084.

Tucholke, B.E., Stewart, W.K., Kleinrock, M.C., 1997. Long-term denudation of ocean crust in the central North Atlantic Ocean. Geology 25 (2), 171–174.

Tucholke, B.E., 1992. Massive submarine rockslide in the rift-valley wall of the mid-Atlantic Ridge. Geology 20, 129–132.

Whitmarsh, R.B., Laughton, A.S., 1976. A long-range study of the Mid-Atlantic Ridge crest near 37°N (FAMOUS area) and tectonic implications. Deep Sea Res. 25, 1005–1023.